Proceedings of Magneto-Optical Recording International Symposium '91, J. Magn. Soc. Jpn., Vol. 15, Supplement No. S1 (1991), pp. 299-306

DYNAMICS OF MAGNETIZATION REVERSAL IN AMORPHOUS FILMS OF RARE EARTH-TRANSITION METAL ALLOYS (Invited)

R. GILES and M. MANSURIPUR*

College of Engineering, Boston University, Boston, Massachusetts 02215, USA
**Optical Sciences Center, University of Arizona, Tucson, Arizona 85721, USA*

Abstract - Computer simulations of a two-dimensional lattice of magnetic dipoles are performed on the *Connection Machine*. The 256 x 256 hexagonal lattice is a discrete model for thin films of amorphous rare earth-transition metal (RE-TM) alloys, which have application as the storage media in erasable optical data storage systems. In these simulations the dipoles follow the dynamic equation of Landau-Lifshitz-Gilbert under the influence of an effective field arising from local anisotropy, near-neighbor exchange, classical dipole-dipole interactions, and an externally applied field. Using mean-field theory, we have calculated the temperature dependencies of the subnetwork magnetizations, the effective fields, the gyromagnetic coefficient, and the Gilbert damping parameter. These results are then used in the simulation of the thermomagnetic recording process, where a focused laser beam creates a hot spot and allows an external magnetic field to reverse the direction of local magnetization. The onset of nucleation and the dynamics of growth/contraction by domain wall motion have been studied by means of these simulations.

KEYWORDS: MAGNETIZATION DYNAMICS, THERMOMAGNETIC RECORDING, DOMAIN NUCLEATION

BACKGROUND

The processes of magnetization reversal in thin amorphous films of rare earth-transition metal alloys play the central role in the recording and erasure of information in erasable optical data storage systems. A major goal of our research effort over the past several years has been the understanding of the nanomagnetic processes involved in the nucleation and growth of submicron-size domains within thin film magnetic media. We have based our investigations on computer simulations of large arrays of interacting dipoles, following the dynamic equation of Landau, Lifshitz and Gilbert (commonly referred to as the LLG equation) [1,2]. The massive parallelism of the *Connection Machine* which allows each dipole to be associated with a separate processor, combined with the Fourier transform algorithm [3,4] for computing the demagnetizing field, have made such large-scale simulations possible [5].

In previous publications [5,6] we reported the effect of local random axis anisotropy on nucleation coercivity. "Local" in this context means that each cell of the lattice is randomly and independently assigned an easy axis within a cone of allowed directions around the perpendicular Z axis. Under such conditions, it was found that the fields required for the nucleation of reverse-magnetized domains were generally higher than those observed in practice. Various submicron-size "defects" were then introduced in the magnetic state of the lattice and the values of coercivity corresponding to different types, sizes, and strengths of these defects were computed. A typical defect is a few hundred angstroms in diameter and has one of the following characteristics: larger (or smaller) than average anisotropy constant, tilted easy axis away from the normal, no magnetic moment (i.e., void), weak exchange coupling to its neighbors at the boundaries, etc. To give an example, voids were found to have insignificant effects on nucleation coercivity, whereas reverse-magnetized seeds, formed and stabilized in areas with large local anisotropy, could substantially reduce the value of the critical field for nucleation.

Random axis anisotropy and magnetic defects also create barriers to domain wall motion. These barriers are overcome only when sufficiently large magnetic fields (in excess of the so-called wall coercivity) are applied. The various aspects of wall coercivity were the subject of another previous publication [7]. Again to give an example, we found that unlike nucleation, wall motion coercivity is significantly modified in the presence of voids. The simulation results indicated a tendency for the voids to attract and pin the walls. It was also revealed through these simulations that wall coercivity in amorphous RE-TM alloy films is generally lower than the corresponding nucleation coercivity, in agreement with the experimentally observed square shape of the hysteresis loops in these media.

In the present paper we report results of simulations of the thermomagnetic recording process. Here the presence of a temperature profile adds another level of complexity to the problem. Magnetic properties of the materials of interest in optical data storage are strong functions of temperature. Some characteristics (such as M_s and K_u) can be measured directly, while others (such as A_x) must be obtained from model calculations. Mean-field theory [8] has been employed to match model parameters with the available experimental data, and to extract from them the temperature-dependencies of the "hidden" characteristics. Figure 1 shows the temperature dependence of the various material parameters used in these simulations; for concreteness, we have confined attention to *a* $Tb_{22}(FeCo)_{73}Ar_5$ alloy material. The saturation magnetization M_s and the individual subnetwork magnetizations M_{RE} and M_{TM} are shown in Fig. 1(*a*). The material has a compensation point at T = 250 K and its Curie point temperature is T_c = 441 K. Figure 1(*b*) shows the material's anisotropy energy constant K_u and its exchange stiffness coefficient A_x versus temperature. The inset is a plot of the effective anisotropy field $H_k = 2K_u/M_s$ versus T in the vicinity of the Curie point; we shall return to this curve later and point out its significance in conjunction with the nucleation process.

From the curves of $K_u(T)$ and $A_x(T)$ one can easily derive the curves of Fig. 1(*c*) which show the wall-energy-density σ_w and the wall-width Δ_w as functions of T. Although σ_w and Δ_w are not needed for the simulations, they are nonetheless important characteristics of the material and we shall have occasion to use them for the analysis of the results. Note in particular that the wall-width is rather weakly dependent on T, going from about 200 Å at the room temperature to about 250 Å just below the Curie point. Finally, Fig. 1(*d*) shows plots of the effective gyromagnetic ratio γ_{eff} and damping coefficient α_{eff} versus temperature. These parameters are obtained from a generalization of the LLG equation to ferri-magnetic systems with strongly coupled magnetic subnetworks; details of this generalization are described in the next section. The third section is devoted to the thermomagnetic simulation results and their discussion. Closing remarks and final thoughts appear in the last section. An appendix is added at the end to clarify the relationship between A_x and the effective exchange field H_{xhg} which acts on individual dipoles of a hexagonal lattice.

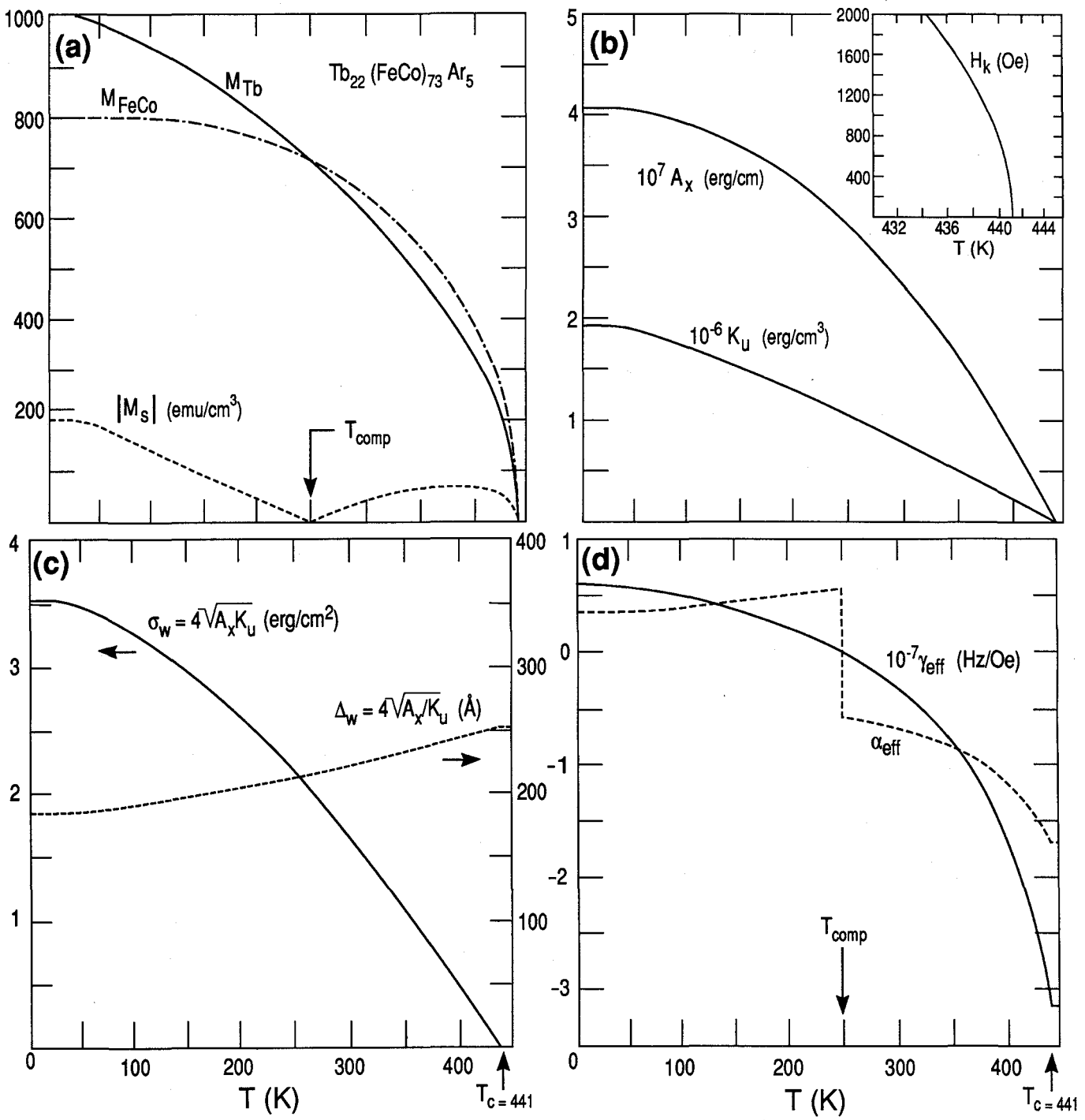

Fig. 1. Temperature dependence of the various magnetic parameters of amorphous $Tb_{22}(FeCo)_{73}Ar_5$, used as recording medium in the computer simulations. (*a*) Saturation and subnetwork magnetizations. (*b*) Anisotropy and exchange coefficients. The inset shows the effective anisotropy field H_k in the vicinity of the Curie point. (*c*) Domain wall energy density and wall-width. (*d*) Effective gyromagnetic ratio γ_{eff} and Gilbert damping parameter α_{eff}. These are calculated from Eqs. (4) and (5) assuming $\gamma_1 = g_1\mu_B/\hbar$, $\gamma_2 = g_2\mu_B/\hbar$ and $\alpha_1 = \alpha_2 = 0.1$. Subnetwork magnetizations $m_1(T)$ and $m_2(T)$ were obtained from the mean-field theory.

DYNAMIC EQUATION FOR STRONGLY-COUPLED FERRIMAGNETS

Consider a thin magnetic film consisting of two antiferromagnetically coupled subnetworks. Let $\mathbf{m}_1$ denote the magnetization vector of the first subnetwork. The magnitude of this vector will be denoted by m_1 (where $m_1 \geq 0$) and the unit vector parallel to $\mathbf{m}_1$ will be identified as $\boldsymbol{\mu}_1$. The gyromagnetic ratio for the first subnetwork is γ_1, and the corresponding Gilbert damping parameter is α_1. Similarly $\mathbf{m}_2$, $\boldsymbol{\mu}_2$, m_2, γ_2 and α_2 represent the second subnetwork ($m_2 \geq 0$).

Let $H_0\mathbf{m}_2$ (where $H_0 \leq 0$) be the effective local exchange field of the second subnetwork on the first. Similarly, $H_0\mathbf{m}_1$ is the effective local exchange field of the first subnetwork on the second. The remaining effective fields on the moments of the two subnetworks shall be denoted by $\mathbf{H}_1$ and $\mathbf{H}_2$, respectively. Under these circumstances the LLG equations for the local dipole moments of individual subnetworks are written

$$\dot{\mathbf{m}}_1 = -\gamma_1 \mathbf{m}_1 \times (\mathbf{H}_1 + H_0\mathbf{m}_2) + \alpha_1 \mathbf{m}_1 \times \dot{\boldsymbol{\mu}}_1 \qquad (1)$$

$$\dot{\mathbf{m}}_2 = -\gamma_2 \mathbf{m}_2 \times (\mathbf{H}_2 + H_0\mathbf{m}_1) + \alpha_2 \mathbf{m}_2 \times \dot{\boldsymbol{\mu}}_2 \qquad (2)$$

Proceedings of Magneto-Optical Recording International Symposium '91, J. Magn. Soc. Jpn., Vol. 15, Supplement No. S1 (1991), pp. 299-306

The superscript dot here and henceforth indicates the time derivative. If H_0 is sufficiently large, the two moments $\mathbf{m}_1$ and $\mathbf{m}_2$ will remain strongly coupled and antiparallel at all times. In this case we define a net moment for the ferrimagnetic material along the unit vector $\boldsymbol{\mu}$ with a magnitude equal to (m_1-m_2). Obviously $\boldsymbol{\mu} = \boldsymbol{\mu}_1 = -\boldsymbol{\mu}_2$. Equations (1) and (2) are now combined to yield

$$\left(\frac{m_1}{\gamma_1} - \frac{m_2}{\gamma_2}\right)\dot{\boldsymbol{\mu}} = -\boldsymbol{\mu} \times (m_1\mathbf{H}_1 - m_2\mathbf{H}_2)$$

$$+ \left(\frac{\alpha_1 m_1}{\gamma_1} + \frac{\alpha_2 m_2}{\gamma_2}\right)\boldsymbol{\mu} \times \dot{\boldsymbol{\mu}} \qquad (3)$$

It is now possible to define net effective values for γ, α and $\mathbf{H}$ as follows :

$$\gamma_{\text{eff}} = \frac{m_1 - m_2}{\frac{m_1}{\gamma_1} - \frac{m_2}{\gamma_2}} \qquad (4)$$

$$\alpha_{\text{eff}} = \frac{\frac{\alpha_1 m_1}{\gamma_1} + \frac{\alpha_2 m_2}{\gamma_2}}{\frac{m_1}{\gamma_1} - \frac{m_2}{\gamma_2}} \qquad (5)$$

$$\mathbf{H}_{\text{eff}} = \frac{m_1\mathbf{H}_1 - m_2\mathbf{H}_2}{m_1 - m_2} \qquad (6)$$

Replacing in Eq. (3) the effective values just defined, one obtains

$$\dot{\boldsymbol{\mu}} = -\gamma_{\text{eff}}\,\boldsymbol{\mu} \times \mathbf{H}_{\text{eff}} + \alpha_{\text{eff}}\,\boldsymbol{\mu} \times \dot{\boldsymbol{\mu}} \ . \qquad (7)$$

At first glance there appears to be two singularities associated with the above equation. The first singularity occurs at the angular momentum compensation, where $m_1/\gamma_1 = m_2/\gamma_2$. Since both γ_{eff} and α_{eff} are infinite at this point, $\boldsymbol{\mu}$ aligns itself with the local effective field instantaneously and without gyration. The second singularity arises at the magnetization compensation, where $m_1 = m_2$. Here $\gamma_{\text{eff}} = 0$ and $\mathbf{H}_{\text{eff}}$ is infinite. However, as will be shown below, the product of γ_{eff} and $\mathbf{H}_{\text{eff}}$ turns out to be finite. The LLG equation for the tightly coupled ferrimagnet in Eq. (7) is thus free from physical singularities and describes the dynamic behavior of the net magnetic moment unambiguously.

We now proceed to express the effective field in Eq. (6) in terms of its four components, namely, the externally applied field $\mathbf{H}^{\text{ext}}$, the demagnetizing field $\mathbf{H}^{\text{dmag}}$, the anisotropy field $\mathbf{H}^{\text{anis}}$, and the exchange field $\mathbf{H}^{\text{xhg}}$. The effective field is thus written

$$\mathbf{H}_{\text{eff}} = \frac{m_1}{m_1-m_2}\left[\mathbf{H}_1^{\text{ext}} + \mathbf{H}_1^{\text{dmag}} + \mathbf{H}_1^{\text{anis}} + \sum_{\substack{\text{nearest}\\ \text{neighbors}}} \mathbf{H}_1^{\text{xhg}}\right]$$

$$- \frac{m_2}{m_1-m_2}\left[\mathbf{H}_2^{\text{ext}} + \mathbf{H}_2^{\text{dmag}} + \mathbf{H}_2^{\text{anis}} + \sum_{\substack{\text{nearest}\\ \text{neighbors}}} \mathbf{H}_2^{\text{xhg}}\right] \qquad (8)$$

The external field is the same for both subnetworks, that is, $\mathbf{H}_1^{\text{ext}} = \mathbf{H}_2^{\text{ext}}$. Similarly, $\mathbf{H}_1^{\text{dmag}} = \mathbf{H}_2^{\text{dmag}}$. As for the field of anisotropy, we assume that both subnetworks have uniaxial magnetic anisotropy along the same unit vector $\mathbf{n}$, but with different anisotropy constants K_{u1} and K_{u2}, respectively. Thus

$$\mathbf{H}_1^{\text{anis}} = \frac{2K_{u1}}{m_1}(\boldsymbol{\mu}_1 \cdot \mathbf{n})\,\mathbf{n} \qquad (9)$$

$$\mathbf{H}_2^{\text{anis}} = \frac{2K_{u2}}{m_2}(\boldsymbol{\mu}_2 \cdot \mathbf{n})\,\mathbf{n} \qquad (10)$$

Next, let us assume that the magnetization of the film is represented by a two dimensional hexagonal lattice of dipoles. It is shown in the Appendix that the effective exchange field exerted on a given dipole by the dipole in a near-neighbor cell may be written as

$$\mathbf{H}_1^{\text{xhg}} = +\frac{4A_{x1}}{3m_1 d^2}\,\boldsymbol{\mu}_{\text{n.n.}} \qquad (11)$$

$$\mathbf{H}_2^{\text{xhg}} = -\frac{4A_{x2}}{3m_2 d^2}\,\boldsymbol{\mu}_{\text{n.n.}} \qquad (12)$$

where $\boldsymbol{\mu}_{\text{n.n.}}$ is the direction of the magnetic moment of the near-neighbor dipole, and d is the constant of the (hexagonal) lattice (i.e., center-to-center distance between nearest-neighbor cells). We designate $K_{u1}+K_{u2}$ as the net anisotropy energy K_u and $A_{x1}+A_{x2}$ as the net exchange stiffness coefficient A_x of the ferrimagnetic material. Replacing the above results and definitions into Eq. (8) yields

$$\mathbf{H}_{\text{eff}} = \mathbf{H}^{\text{ext}} + \mathbf{H}^{\text{dmag}} + \frac{2K_u}{m_1 - m_2}(\boldsymbol{\mu} \cdot \mathbf{n})\,\mathbf{n}$$

$$+ \frac{4A_x}{3(m_1 - m_2)d^2} \sum_{\substack{\text{nearest}\\ \text{neighbors}}} \boldsymbol{\mu}_{\text{n.n.}} \qquad (13)$$

Equation (13) is the complete expression for the effective field which, together with Eqs. (4) and (5), provide the parameters of the LLG equation.

RESULTS AND DISCUSSION

The temperature distribution imposed on the lattice has a Gaussian spatial profile, with an exponential rise followed by an exponential fall in time, as shown in Fig. 2. The following equation succinctly describes this temperature profile :

$$T(r, t) = T_0 + (T_{\max} - T_0)\exp\left[-(r/r_0)^2\right] f(t) \qquad (14)$$

In the above equation T_0 is the ambient temperature (T_0 = 300 K), $T_{\max}$ is the maximum temperature reached during the heating cycle ($T_{\max}$ = 500 K), r_0 is the $1/e$ radius of the Gaussian hot spot (r_0 = 1800 Å) which is also related to the full-width-at-half-maximum of the spatial distribution (FWHM = $1.665r_0$ = 0.3 μm), and $f(t)$ is the time-dependence of the temperature profile whose functional form is given in the caption to Fig. 2. This time-dependence is such that at $t = 0$ the lattice is at the uniform temperature of T_0, by $t = t_{\text{peak}}$ = 10 ns the temperature has peaked everywhere with a maximum of $T_{\max}$ at the center of the lattice, and by $t = t_{\text{end}}$ = 20 ns the entire lattice has dropped back to the ambient temperature. For the sake of simplicity we have ignored the effects of heat diffusion and assumed that the spatial temperature profile remains the same at all times. Note also

that the assumed profile is stationary, that is, the center of the hot spot does not move over the lattice. These characteristics are, of course, somewhat artificial, considering the nature of the laser-induced heating processes in actual media. What is more, the assumed pulse duration is relatively short compared to the current practice of thermomagnetic recording. Nonetheless, we believe the neglect of such details to be of little consequence as far as the basic processes of magnetization reversal are concerned.

The two-dimensional lattice in all the simulations had 256 × 256 dipoles with hexagonal lattice cells, periodic boundary conditions, and a lattice constant of d = 10 Å. The area of the simulated lattice is thus 0.256 μm × 0.222 μm. The assumed film thickness, corresponding to the height of each and every cell in the lattice, is h = 500 Å. The imposed temperature distribution with FWHM = 0.3 μm is wider than the lattice itself but, as it turns out, magnetization reversal is confined to the region near the center of the hot-spot and the phenomena of interest therefore occur within the boundary of the lattice. Since the Curie point temperature of the material under consideration is T_c = 441 K, at the peak temperature (occuring at t = 10 ns) the radius of the Curie disk (i.e., the paramagnetic region) is r_c = 1065 Å. The Curie disk first appears at t = 3.4 ns and expands until t = 10 ns, at which point it begins to shrink rapidly and disappears at t = 11 ns.

In the limited number of simulations conducted to date, we have observed that reversal begins by nucleating a domain wall at the rim of the Curie disk. A simple analysis shows that such nucleation is possible only when the externally applied field H_{ext} is greater than the effective anisotropy field H_k within a certain annulus surrounding the Curie disk. Let T_c^- denote a temperature slightly below the Curie point and allow $M_s(T_c^-)$ to be the saturation magnetization at that point.

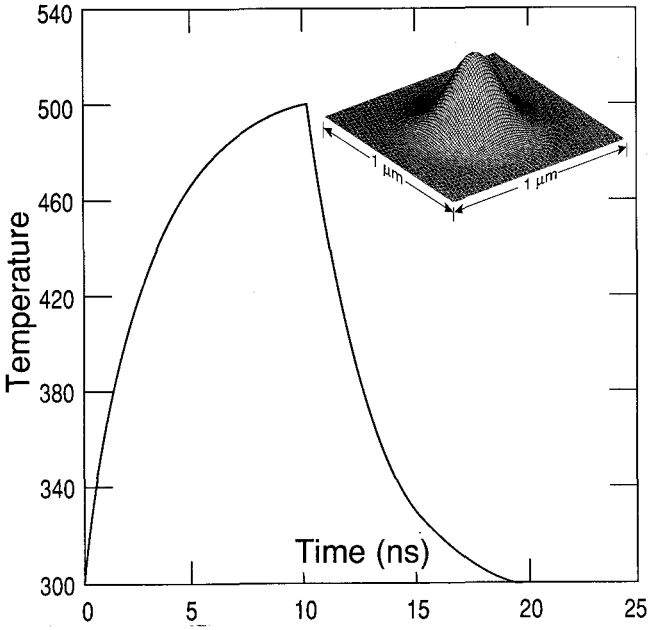

Fig. 2. Temperature distribution on the lattice. The spatial profile is Gaussian with FWHM = 0.3 μm. The temporal profile $f(t)$ is

$$\frac{1 - \exp(-t/\tau_1)}{1 - \exp(-t_{peak}/\tau_1)}; \quad 0 \le t \le t_{peak}$$

$$1 - \frac{1 - \exp[(t_{peak} - t)/\tau_2]}{1 - \exp[(t_{peak} - t_{end})/\tau_2]}; \quad t_{peak} \le t \le t_{end}.$$

In the particular case shown here t_{peak} = 10 ns, t_{end} = 20 ns, and $\tau_1 = \tau_2$ = 3 ns.

Similarly denote the corresponding value of the wall energy density by $\sigma_w(T_c^-)$ and that of the wall width by $\Delta_w(T_c^-)$. Ignoring the demagnetizing effects and considering only the balance between wall energy and external-field energy, the formation of a domain wall at the Curie rim requires that the following condition be satisfied :

$$\sigma_w(T_c^-) \le H_{ext}\, M_s(T_c^-)\, \Delta_w(T_c^-) \qquad (15)$$

Replacing for σ_w and Δ_w in terms of K_u and A_x, we find the necessary condition for nucleation as follows :

$$H_{ext} \ge \frac{2\,K_u(T_c^-)}{M_s(T_c^-)} = H_k(T_c^-) \quad . \qquad (16)$$

Typically $H_k(T)$ is a decreasing function which rapidly goes to zero at the Curie point (see the inset in Fig. 1(*b*)). Thus, as one moves away from the curie rim, one finds a sharp increase in H_k. If, however, H_k remains below H_{ext} in the immediate neighborhood of the Curie rim (say, within an annulus of width Δ_w), then the preceding analysis indicates that wall formation is energetically favorable and the nucleation process may therefore commence. Conversely, when H_k at the radius of $r = r_c + \Delta_w$ is greater than H_{ext}, a wall becomes costly in terms of energy and there can be no nucleation.

In light of the above discussion it is clear that the temperature gradient at the Curie rim plays an important role in the nucleation stage of the reversal process. A small gradient at the rim provides for a slow rise in H_k, thus facilitating nucleation. A large gradient, on the other hand, makes the immediate neighborhood of the Curie disk less hospitable to domain walls. In the case of a Gaussian temperature profile with $1/e$ radius of r_0, the maximum gradient occurs at $r = (1/\sqrt{2})\, r_0$. This corresponds in our simulations to r = 1273 Å, which is somewhat greater than the largest radius of the Curie disk attained. Now, a domain formed during the heating cycle (i.e., when $t \le t_{peak}$) must expand rapidly or else it will be consumed by the advancing Curie disk. Nucleation followed by rapid growth during the heating cycle is not impossible but is unlikely, especially when the applied field H_{ext} is relatively weak. The more likely scenario is the formation of a wall (at the Curie rim) during the cooling period, i.e., when $t \ge t_{peak}$. In this event the newly created wall can remain stationary, or even shrink slowly, and yet survive. In addition, the cooling period has the desirable feature that with the advancing of time the temperature gradient at the Curie rim declines, thus rendering nucleation more likely.

In the absence of coercivity mechanisms, such as defects and material inhomogeneities that would pin the domain wall, a domain nucleated in the thermomagnetic process will be unstable. Such domains will either expand or collapse, depending on the energetics of the magnetic medium and the magnitude of the applied field. Since the subject of wall-motion coercivity and the related issue of domain stability have already been addressed in another publication [7], they shall not concern us in this paper. In the remainder of this section we present simulation results that pertain to the formative stages of domain nucleation and the early phases of adjustment (via expansion and/or contraction) during thermomagnetic recording.

Figure 3 shows the state of magnetization of the lattice at several instants of time during the cooling period, with H_{ext} = 500 Oe. The simulation started at t = 10.12 ns, when a shrinking Curie disk had a radius of r_c = 1000 Å. Frame (*a*) in Fig. 3 shows the state of the lattice at t = 10.68 ns. The gray region at the center is above the Curie temperature (in our terminology, the gray region is the Curie disk). The colorful pixels around the rim are the dipole moments which,

Proceedings of Magneto-Optical Recording International Symposium '91, J. Magn. Soc. Jpn., Vol. 15, Supplement No. S1 (1991), pp. 299-306

in anticipation of wall formation, have rotated into the plane of the lattice. The color of each pixel represents the orientation of its dipole. The remaining white pixels are the dipoles which are still in the remanent state, being perpendicular to the lattice and pointing upward. The next Frame, (*b*), shows the state of the lattice at t = 10.92 ns where, in addition to the colorful pixels representing a continuous domain wall, there is a thin black ring surrounding the Curie disk. Black pixels correspond to fully reversed dipoles, that is, they are perpendicular to the lattice and point downward. In Frame (*c*) we show the situation at t = 11 ns, where the Curie disk is about to disappear and leave a reverse-magnetized domain behind. The final Frame (*d*) in this sequence shows a shrinking domain at t = 11.58 ns; apparently the wall-energy-density σ_w is too large for the external and demagnetizing fields to overcome, thus forcing the collapse of the domain. In practice, of course, defects and inhomogeneities of the medium can prevent this collapse (by pinning the wall) and stabilize the domain, even in the absence of the external field.

Another example of the thermomagnetic simulations is given in Fig. 4. The situation here is very similar to that of the previous example, with the exception of the applied field being H_{ext} = 1000 Oe. Frames (*a*)-(*d*) in Fig. 4 correspond to instants of time t = 10.20 ns, 10.60 ns, 10.96 ns and 11.58 ns, respectively. Comparing the results with those of the previous example, we note that the larger field causes nucleation to begin earlier. Also, the domain formed in the latter case is more likely to be stable, since the larger H_{ext} seems to have successfully counteracted the inclination of the wall to collapse.

CLOSING REMARKS

Thermomagnetically recorded domains on a uniform lattice are unstable and either expand or collapse at the end of the write cycle. On the other hand, real materials are nonuniform; the large coercivities exhibited by them is but one manifestation of their nonuniformity. We introduced coercivity mechanisms in the simulated lattice and studied the recording process in the presence of various defects and inhomogeneities. Spatial fluctuations of the magnetic parameters (such as the directions of the local easy axes) from one lattice cell to another were found to have little effect, if any, on the stability of the domains. This is understandable in light of the fact that wall-width in amorphous RE-TM alloys is of the order of 100 Å, whereas the lattice constant is only 10 Å; the fluctuations are therefore averaged out. When spatial fluctuations and material inhomogeneities were distributed over patches of random shape and size (average patch diameter $\simeq$ several hundred angstroms), they proved to be successful in pinning the domain walls, thus stabilizing the recorded domains.

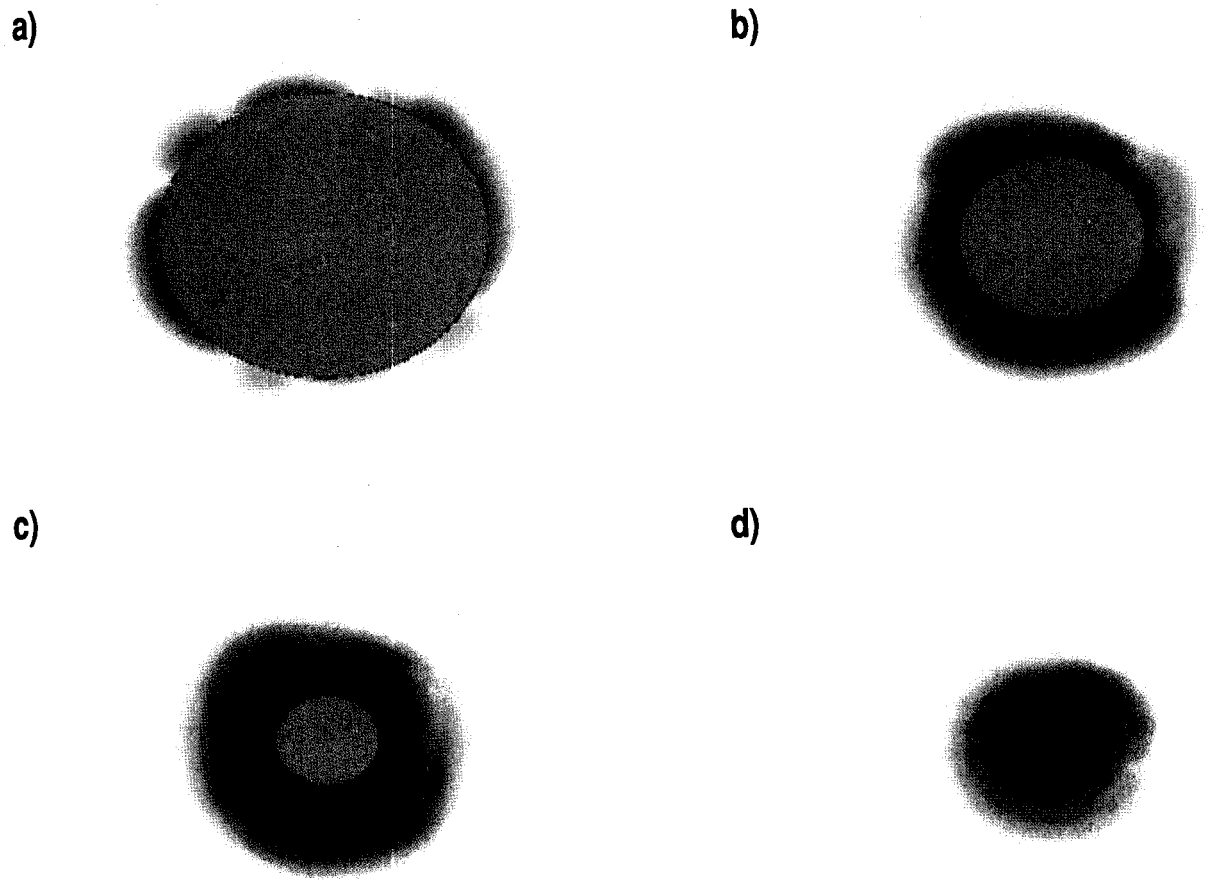

Fig. 3. Snap-shots from the state of magnetization of the lattice during the cooling period. The magnitude of the external field is H_{ext} = 500 Oe. The white (black) pixels are magnetized perpendicular to the plane of the lattice and point upward (downward), the central gray region is above the Curie temperature, and the colored pixels have magnetization in the plane (or inclined towards the plane) of the lattice. (*a*) t = 10.68 ns. (*b*) t = 10.92 ns. (*c*) t = 11 ns. (*d*) t = 11.58 ns.

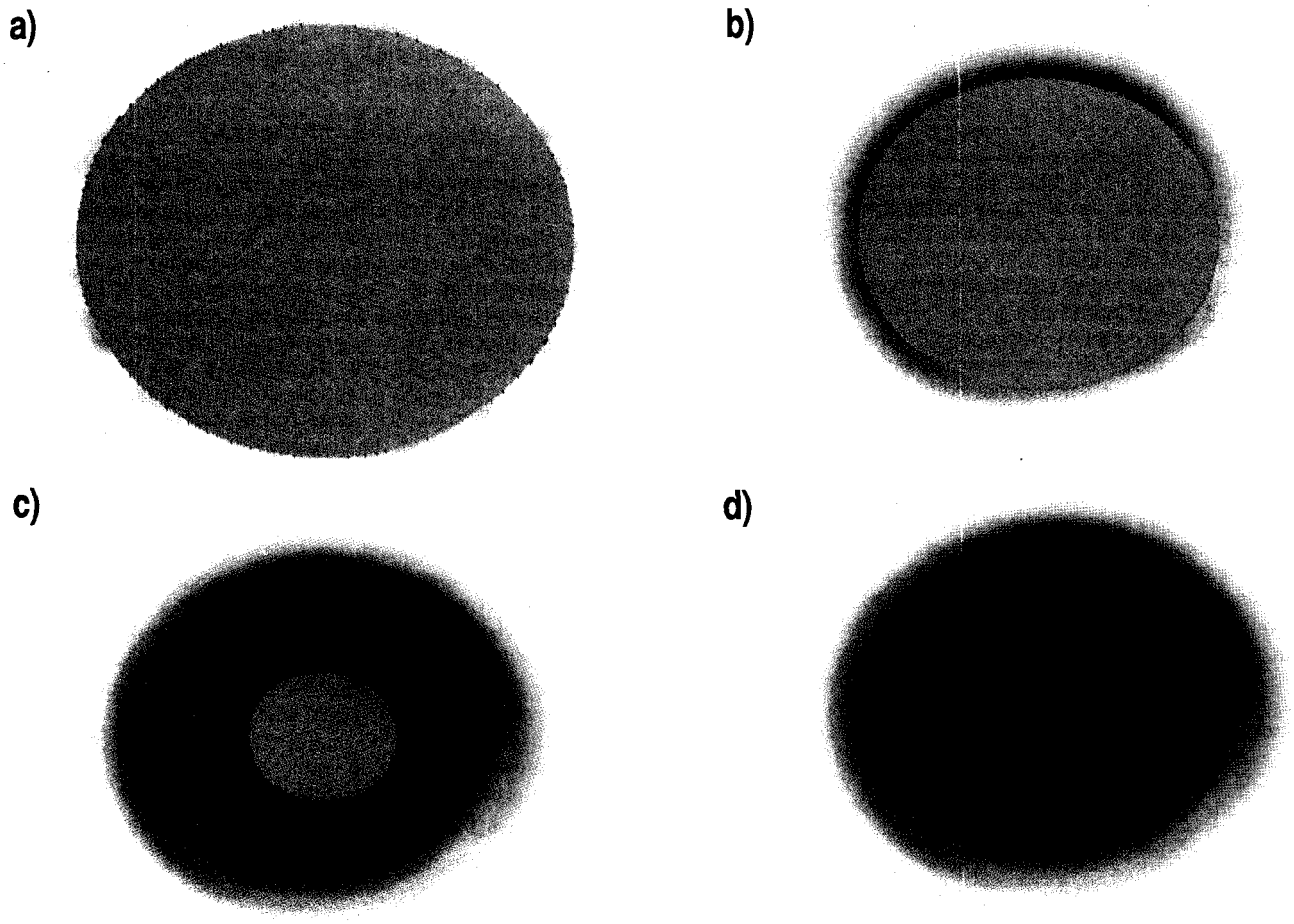

Fig. 4. Same as Fig. 3 but with H_{ext} = 1000 Oe. (*a*) t = 10.20 ns. (*b*) t = 10.60 ns. (*c*) t = 10.96 ns. (*d*) t = 11.58 ns.

ACKNOWLEDGEMENT

This work has been supported by a grant from the IBM Corporation and, in part, by the Optical Data Storage Center at the University of Arizona.

APPENDIX

Consider a thin magnetic film parallel to the XY plane, with finite thickness h and magnetization distribution $\mathbf{m}(x,y)$. Notice that $\mathbf{m}$ is independent of z, implying that the magnetization is uniform throughout the film thickness. Moreover, we shall assume that the magnitude of the magnetization is constant everywhere, and denote this constant value by m. Thus the spatial variations of $\mathbf{m}(x,y)$ are due to its orientation variations only. We define the unit-magnitude field $\boldsymbol{\mu}(x,y) = \mathbf{m}(x,y)/m$ and let the exchange stiffness coefficient of the film over the region of interest be A. The exchange energy E_{xhg} of the film is then given by

$$E_{xhg} = h\,A \iint \left[(\nabla \mu_x)^2 + (\nabla \mu_y)^2 + (\nabla \mu_z)^2 \right] dxdy \,. \quad \text{(A1)}$$

Our next task is to relate the exchange energy, expressed in Eq. (A1) as an integral over a continuum, to the discrete distribution of dipoles on a hexagonal lattice. Assume that the lattice constant is d and let (x_0, y_0) be the center of an arbitrary lattice cell. The dipole moment associated with this cell will be denoted by $\mathbf{m}_0$ where

$$\mathbf{m}_0 = \frac{\sqrt{3}d^2h}{2}\,\mathbf{m}(x_0, y_0) \quad \text{(A2)}$$

In a similar fashion, define the six nearest neighbors of $\mathbf{m}_0$ and denote them by $\mathbf{m}_n$, where $1 \le n \le 6$. As before, $\boldsymbol{\mu}_n$ will be a unit vector parallel to $\mathbf{m}_n$. Let $\mathbf{d}_n$ be the vector connecting (x_0, y_0) to the center of its near-neighbor cell at (x_n, y_n). Clearly, the magnitude of $\mathbf{d}_n$ is equal to the lattice constant d for $1 \le n \le 6$. One then writes

$$\boldsymbol{\mu}_n - \boldsymbol{\mu}_0 \simeq (\nabla \mu_x \cdot \mathbf{d}_n)\,\hat{x} + (\nabla \mu_y \cdot \mathbf{d}_n)\,\hat{y} + (\nabla \mu_z \cdot \mathbf{d}_n)\,\hat{z} \quad \text{(A3)}$$

Forming the dot product of Eq. (A3) with itself, one obtains

$$2 - 2\,\boldsymbol{\mu}_n \cdot \boldsymbol{\mu}_0 \simeq (\nabla \mu_x)^2\, d^2 \cos^2\Theta_n + (\nabla \mu_y)^2\, d^2 \cos^2\Phi_n + (\nabla \mu_z)^2\, d^2 \cos^2\Omega_n \quad \text{(A4)}$$

In the above equation Θ_n, Φ_n, Ω_n are the angles between $\nabla\mu_x$, $\nabla\mu_y$, $\nabla\mu_z$ and $\mathbf{d}_n$, respectively. Summing Eq. (A4) over the six nearest neighbors of $\mathbf{m}_0$ yields

$$-2 \sum_{n=1}^{6} \boldsymbol{\mu}_n \cdot \boldsymbol{\mu}_0 \simeq d^2 \left\{ (\nabla \mu_x)^2 \sum_{n=1}^{6} \frac{1 + \cos 2\Theta_n}{2} + (\nabla \mu_y)^2 \sum_{n=1}^{6} \frac{1 + \cos 2\Phi_n}{2} + (\nabla \mu_z)^2 \sum_{n=1}^{6} \frac{1 + \cos 2\Omega_n}{2} \right\} + \text{constant} \quad \text{(A5)}$$

Proceedings of Magneto-Optical Recording International Symposium '91, J. Magn. Soc. Jpn., Vol. 15, Supplement No. S1 (1991), pp. 299-306

Thanks to the symmetry of the problem, sums of cosines in all cases turn out to be zero. Multiplying the remaining terms in Eq. (A5) by the constant factor $2A/3d^2$ results in

$$-\left[\frac{4A}{3d^2}\sum_{n=1}^{6}\mu_n\right]\cdot\mu_0 \simeq 2A\left[(\nabla\mu_x)^2+(\nabla\mu_y)^2+(\nabla\mu_z)^2\right] + \text{constant} \qquad \text{(A6)}$$

The right-hand-side of Eq. (A6) is the exchange energy density of the interaction between $\mathbf{m}_0$ and its nearest neighbors. (Note the factor of 2 that has been included in this expression in order to account for the interactions in both directions.) The effective exchange field acting on $\mathbf{m}_0$ is thus found to be

$$\mathbf{H}_{xhg} = \frac{4A}{3m_0 d^2}\sum_{n=1}^{6}\mu_n \qquad \text{(A7)}$$

This is the desired result, relating the exchange stiffness parameter A of the continuum formulation to the effective exchange field on individual dipoles of the discrete hexagonal lattice.

REFERENCES

1. A. P. Malozemoff and J. C. Slonczewski, *Magnetic Domain Walls in Bubble Materials*, Academic Press, New York, 1979.
2. M. Mansuripur, J. Appl. Phys. **63**, 5809 (1988).
3. M. Mansuripur and R. Giles, IEEE Trans. Magnet. **24**, 2326 (1988).
4. M. Mansuripur, J. Appl. Phys. **66**, 3731 (1989).
5. M. Mansuripur and R. Giles, *Computers in Physics* **4**, 291 (1990).
6. R. Giles and M. Mansuripur, *Computers in Physics* **5**, 204 (1991).
7. M. Mansuripur, R. Giles and G. Patterson, J. Mag. Soc. Japan **15**, 17 (1991).
8. M. Mansuripur and M. F. Ruane, IEEE Trans. Magnet. **22**, 33 (1986).